Preparation and properties of lightweight and high-strength building ceramsites with oil-based drilling cuttings pyrolysis residues

Hongjuan Wang[1,2], Jing Li[1,2], Dong Lin[1,2], Guobing Jiang[1,2], Liang Zhao[1,2], Jinlei Yu[1,2], Tian Meng[1,2], Xinyu Huang[1,2], Hongwu Liu[3] and Yuanyi Yang[3,4]*

[1]Safety and Technology Supervision Research Institute of PetroChina Southwest Oil and Gas Field Company, Chengdu, China, [2]Shale Gas Evaluation and Exploitation Key Laboratory of Sichuan Province, Chengdu, China, [3]School of Civil Engineering and Geomatics, Southwest Petroleum University, Chengdu, China, [4]Research Institute of Engineering Safety Assessment and Protection of Southwest Petroleum University, Chengdu, China

With the continuing advancement in China's exploration and development technologies of shale gas resources, there was a significant increase in shale gas oil-based drilling cuttings. In this paper, oil-based drilling cutting pyrolysis residues (ODCPRs) was used as the main raw material for preparing lightweight and high-strength building ceramsites to eliminate the environmental risks and recycle industrial waste. Firstly, orthogonal experiments were used to study the influences of raw material composition, preheating temperature, preheating time, sintering temperature, and sintering time on the properties of building ceramsites. From the results, the sintering temperature and the content of ODCPRs were discovered to be the key factors affecting the sintering process of ceramsites. Secondly, the influences of sintering temperature and heating rate on the properties of building ceramists were further explored to find the optimum sintering conditions. When the content of ODCPRs in the ceramsite was set to be 50%, the obtained building ceramsites presented excellent properties with particle compressive strength of 6.31 MPa, bulk density of 575.11 kg/m^3, apparent density of 1097.24 kg/m^3, and the water absorption of 1.89%. Finally, XRD, SEM, TG-DSC, and heavy metal leaching experiments were comprehensively conducted to analyze the composition structure variation and sintering mechanism of the building ceramsite. This paper presents an approach for the recycling, utilization, and disposal of oil-based drilling cuttings in the oil field waste management.

KEYWORDS

oil-based drilling cutting pyrolysis residues, building ceramsite, sintering reaction, lightweight, high-strength

1 Introduction

In recent years, natural gas as a clean energy source is increasingly favored in China's energy consumption structure, which greatly stimulates the exploration and development of shale gas. To prevent wellbore collapse during the shale gas extraction process, a significant amount of oil-based drilling mud is typically used, which in turn generates substantial quantities of oil-based drilling cuttings. Due to the high concentration of petroleum

pollutants, phenolic compounds, heavy metals, and other toxic substances contained in the cuttings, the environmental and safe disposal measures of oil-based drilling cutting present a remarkable challenge (Chaillan et al., 2006; Xiong and Wang, 2021). Currently, due to the high efficiency in recovering oil-based substances and low pollution risk during the treatment process, the pyrolysis treatment technology is the only large-scale industrial implementation method for oil-based drilling cuttings (Kingman et al., 2009; Abnisa and Alaba, 2021; Du et al., 2021; Mishra et al., 2021). However, the residual solid phases of oil-based drilling cuttings after pyrolysis may still contain trace amounts of petroleum hydrocarbons and partially dissolved heavy metal ions, thereby presenting persistent environmental risks. The substantial accumulation of oil-based drilling cutting pyrolysis residues (ODCPRs) not only occupied valuable land resources but also posed a significant threat to the environment (Ball et al., 2012; Owens and Santner, 2021; Li et al., 2022). Thus, there is still a need to explore and study effective ways to utilize ODCPRs as a valuable resource by eliminating environmental risks, increasing industrial additional value, and reducing production costs at the same time.

Extensive research is conducted on the resource utilization of ODCPRs, such as the raw materials applied in road fillers (Xiong and Wang, 2021), sintered bricks (Wang et al., 2017), non-sintered bricks (Liu et al., 2018; Wang et al., 2019), concrete (Bernardo et al., 2007; Foroutan et al., 2018), and glass ceramics (Abbe et al., 2009). Besides, the ODCPR content in these materials typically does not exceed 10% to ensure product quality, resulting rather low utilization rate of ODCPRs. Due to the low utilization of this alternative raw material, there is still a potential for applications needed. Therefore, it is still an important goal for addressing the massive accumulation of ODCPRs to find a resource utilization approach with higher ODCPRs consumption, lower costs, and broader applications.

Lightweight ceramsites, as an artificial lightweight aggregate with a hard surface and porous structure inside, are widely used in construction, environmental industries, and other fields owing to their characteristics of lightweight, thermal insulation, and excellent durability (He et al., 2015; Ji et al., 2015; Xie et al., 2016; Lau et al., 2017; Zhao et al., 2018; Hao et al., 2019). The raw materials for normal building ceramsites mainly include natural minerals such as shale and clay (Başaran Bundur et al., 2017; Ahmad and Chen, 2019; Omar Ahmed and Hassan Assem, 2021). However, with the depletion of natural mineral resources and the increasingly stringent environmental regulations, industrial wastes were becoming a substitute for natural raw materials in the building ceramsite production. The reported industrial solid wastes that have been used for the preparation of building ceramsites include tailings (Wang et al., 2014; Li et al., 2020), municipal sludge (Qi et al., 2009), red mud (RM) (Mi et al., 2021; Mi et al., 2022), and fly ash (FA) (Qin et al., 2015), which contain abundant silicon-aluminum components to obtain good properties. Meanwhile, previous studies indicate that ODCPRs have similar components to ordinary industrial solid wastes, which was also a proper candidate to generate sintering ceramsites. Thereinto, Liu et al. (2023) prepared a high-strength and low-density ceramsite proppant using 20% ODCPRs and 76% bauxite, with a denser structure and a breakage ratio of 8.6% under a closure pressure of 52 MPa after sintering at 1342°C. Yang et al. (2022) successfully prepared a low-density ceramsite proppant by utilizing a mixture of

30% water-based drilling cuttings and 70% bauxite after sintering at 1420°C with a breakage ratio lower than 5% under a closure pressure of 52 MPa. The aforementioned studies have demonstrated the potential for producing building ceramsites using ODCPRs, however, there is limited literature available on the preparation of lightweight and high-strength building ceramsites with ODCPRs.

The goal of this study is to prepare high-performance lightweight and high-strength building ceramsites with ODCPRs as the main raw material. Meanwhile, FA, RM, and quartz sand (QS) are taken as auxiliary materials, and SiC was a foaming agent. The influences of ODCPRs ratios and sintering procedures (preheating temperature, preheating time, sintering temperature, sintering time, and heating rate) on the properties of the ceramsites are systematically investigated, and the optimal sintering condition and formula are obtained, providing a new solution for approach in the resource utilization and industrial the waste utilization and disposal of solid waste co-disposal of oil-based drilling cuttings.

2 Experimental materials and methods

2.1 Raw materials

ODCPRs were obtained from a shale gas field in Southwest China, FA was collected from a power plant in Tangshan, Hebei, QS was provided by Chongqing Changjiang Group Co., Ltd., RM was obtained from Shandong, and the SiC foaming agent was purchased from Shanghai Macklin Biochemical Co., Ltd.

Different test methods were conducted on the raw materials to obtain the basic information. Firstly, X-ray diffraction (XRD) was used to analyze the phase composition of the raw materials. The results were shown in Supplementary Figure S1, indicating that the phases of ODCPRs included quartz, barite, calcite, and dolomite. The phases of FA contained quartz, mullite, and hematite. The main phases of RM included calcite, quartz, hematite, and boehmite; and the phases of QS were quartz and microcline.

X-ray fluorescence (XRF) spectrometer was utilized to determine the chemical compositions of all experimental raw materials, with the results shown in Supplementary Table S1. It can be observed that ODCPRs show relatively low contents of Si and Al as 38.53% and 17.87%, respectively. Additionally, other mineral elements such as Ca, Fe, and Ba were present, particularly with high concentrations of Ba and Ca, which would significantly impact the sintering process of the building ceramsites. Meanwhile, FA and QS were selected as auxiliary sintering materials to supply the silicon-aluminum phase in the raw materials. Furthermore, a small amount of RM was added caused of its property of containing iron phases that could be used as a foaming agent at relatively high temperatures, reducing the density of the ceramsite, and also serving as a flux component during granulation (Mi et al., 2021; Mi et al., 2022). According to Riley's ternary phase diagram (Riley, 1951), the content of SiO_2, Al_2O_3, and fusing components in the green body should be controlled within a certain range, in order to achieve a good sintering performance for preparation of the ceramsite. The content of SiO_2 should be controlled within 48%–78%, Al_2O_3 content should be controlled at 10%–25%, and the content of the fusible component is 13%–26%, which was aimed at achieving good expansion and mechanical performance (Yang et al., 2005; Tsai et al., 2006). At present, many studies (Wang
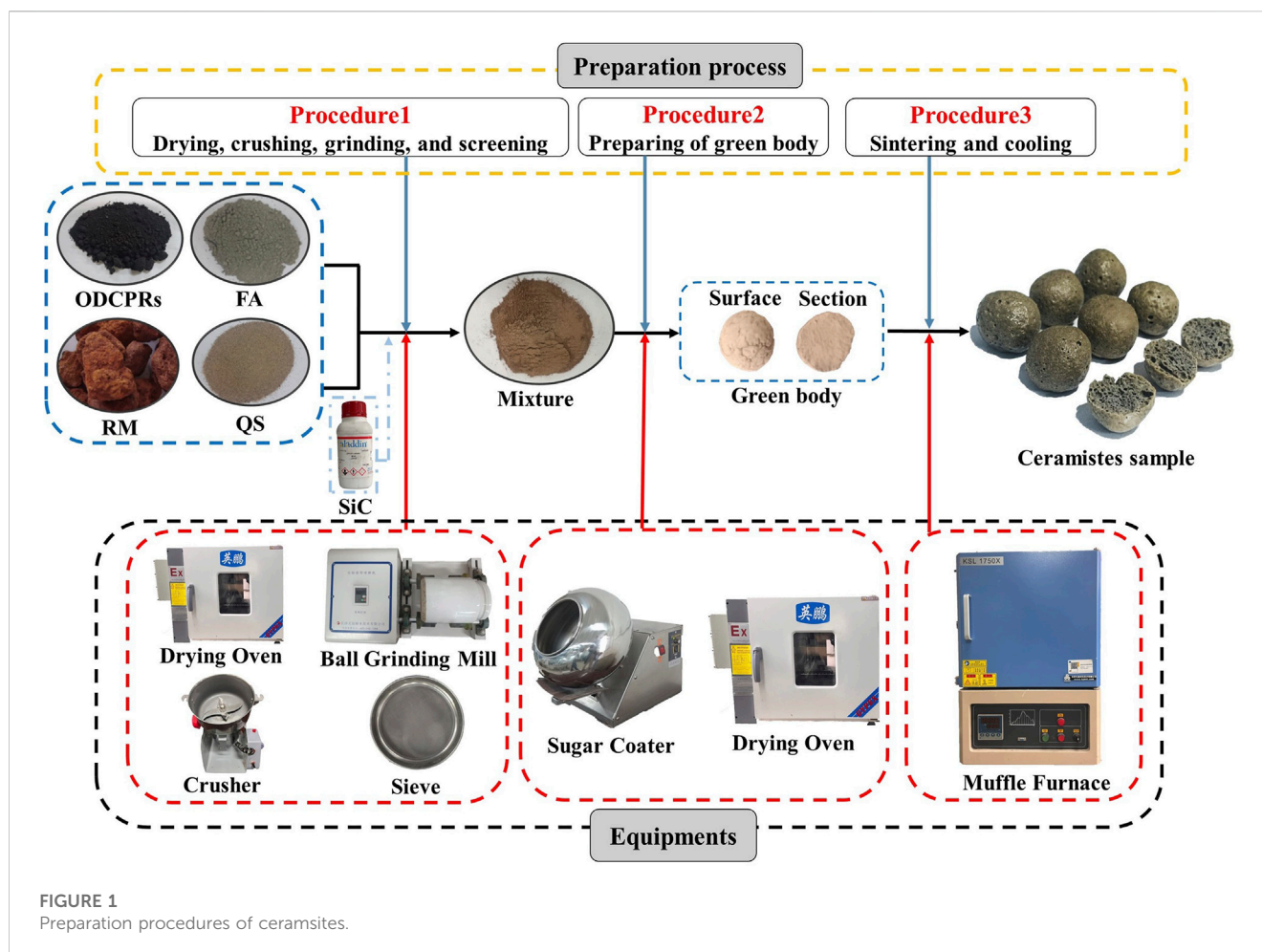
FIGURE 1
Preparation procedures of ceramsites.

et al., 2020; Mi et al., 2021; Zhuo et al., 2023) have successfully used solid waste to prepare lightweight and high-strength ceramics by adjusting raw materials within the range of chemical components. Hence, the calculated ingredient proportions of ceramsites in our study were specified in Supplementary Table S2 and in Supplementary Figure S2, where the ODCPRs content ranged from 30% to 60%.

Through TG-DSC analysis, the physical and chemical reactions of raw materials (ODCPRs, FA, RM, QS and SiC) during the sintering procedure can be obtained, which can provide data support for the enactment of sintering system, with the results shown in Supplementary Figure S3. From Supplementary Figure S3A, ODCPRs exhibited a significant weight loss during the heating process, with a mass loss of over 25.00%, and there were three distinct weight loss temperature regions as "the room temperature to 550°C," "550°C–900°C," and "900°C–1300°C." It was inferred that the first stage involved the combustion of residual water and organic matters, and there was an obvious exothermic effect caused by the oxidation reaction of oil-based organic matter within the range of 350°C–550°C (Jia et al., 2023) (mass loss reached 6.02%); the second stage involved the decomposition of carbonate, with endothermic peaks appearing around 700°C–900°C due to the decomposition of calcite and aragonite, respectively (Maitra et al., 2005) (mass loss reached 10.68%); the third stage corresponded to the decomposition of sulfate and other substances (mass loss reached 7.79%), and the position of the endothermic peak in this temperature range appeared

at 1065°C, corresponding to the generation of the liquid phase and solid-phase reactions at high temperatures (Khalil et al., 2018).

As shown in Supplementary Figure S3B, from the TG results, the overall weight loss of FA was relatively small, only 4.46%, which two weight loss stages at room temperature to 650°C and 650°C–1300°C were observed. The first stage achieved a weight loss of 2.76%, which was inferred from the evaporation of moisture in FA and the combustion of unburnt carbon, while the DSC result indicated that this reaction was an obvious endothermic effect. The second stage achieved a weight loss of 1.70%, which was speculated to be due to the decomposition of hematite. The decomposition temperature of Fe_2O_3 under high temperatures was generally between 800°C and 1550°C. The decomposition reaction occurred in a wide temperature range and belonged to a slow-release type (Mi et al., 2022).

As shown in Supplementary Figure S3C, from the TG results, RM had a relatively larger weight loss of 20.28%, with three distinct weight loss stages at "room temperature to 450°C," "450°C–900°C," and "900°C–1300°C," respectively. The first stage corresponded to the decomposition of bound water and organic matter (mass loss of 10.02%). The second stage corresponded to the dehydration of boehmite (AlO(OH)) and the decomposition of calcite (mass loss of 7.68%). The third stage was due to the decomposition of hematite (mass loss of 2.11%). From the result of DSC curve, the three distinct stages of weight loss were accompanied by clear endothermic effects.

TABLE 1 Sintering parameters design of the orthogonal experiments.

Impact factors	ODCPRs content (%)	Preheating temperature (°C)	Preheating time (min)	Sintering temperature (°C)	Sintering time (min)
	A	B	C	D	E
1	30	350	10	1,070	10
2	40	400	15	1,100	15
3	50	450	20	1,130	20
4	60	500	30	1,160	30

As shown in Supplementary Figure S3D, QS had relatively stable thermal properties with no obvious weight loss steps than other raw materials in the TG curve. The endothermic peak appearing around 1100°C in DSC curve may be due to the transformation of the quartz crystal structure.

As shown in Supplementary Figure S3E, the TG curve of SiC in the temperature range of 0°C–1300°C showed a trend of first decreasing and then increasing, which was mainly related to the oxidation reaction of SiC. The oxidation reaction of SiC was mainly manifested in two parts: passive oxidation characterized by net mass increase and active oxidation characterized by net mass loss (Liang et al., 2021). Therefore, the overall mass showed a trend of first decreasing and then increasing. Simultaneously, SiC provided a sufficient gas phase for the matrix of ceramsite during the oxidation reaction. In addition, the DSC curve showed an overall endothermic trend starting from 300°C, which was related to the reaction of SiC.

2.2 Preparation process of ceramsites

The preparation process of ceramsite was illustrated in Figure 1: ① Raw materials were weighed according to the proportions listed in Supplementary Table S2 and well mixed with a small amount of water. The mixture was then ground by a ball grinding mill (QM-3, Changsha Tianchuang Powder Technology Co., Ltd.) for 1 h. Subsequently, the well-ground and filtered slurry were transferred to a drying oven (BXP-070Gx, Guangzhou Anfei Environmental Protection Technology Co., Ltd.), and dried to constant weight. After that, the filter cake was crushed using a pulverizer (HTY-800, Zhejiang Yongkang Red Sun Electromechanical Co., Ltd.). The crushed powders were fully dispersed and screened through a 0.25 mm sieve. Moreover, a laser particle size analyzer (Master Sizer 2000, Malvern Panalytical Ltd., United Kingdom) was used to test the particle size distribution of the mixed raw powders, as shown in Supplementary Figure S4A, which indicated that the particle size distribution of the grounded raw material powder was ranged from 0.3 to 100 μm, and with a D50 value of 14.91 μm. ② The raw material powder was granulated into a green body with a diameter of 12 mm ± 1 mm using a sugar coater (BY-300, Taizhou GEX Machinery Co., Ltd.). The granulated green bodies were subsequently dried until a constant weight was achieved. ③ The dry green body was sintered at high temperature in a muffle furnace (KSL 1750X, Hefei Kejing Material Technology Co., Ltd.) following the sintering procedure shown in Supplementary Figure S4B. After being cooled to room temperature,

the samples were removed from the furnace and subjected to property testing.

2.3 Physical and chemical properties of building ceramsites

2.3.1 Physical properties

The bulk density (ρ_1, kg/m³), apparent density (ρ_2, kg/m³), and 1 h water absorption ($W_{1\,h}$, %) of the ceramsite were tested according to the Chinese Standard "GB/T 17431.2-2010." Each test group was repeated by three times, and the calculation formulas of different properties were shown as follows:

(1) The bulk density and apparent density

$$\rho_1 = \frac{m}{V_0} \times 1000 \qquad (1)$$

Where m represented the mass (g) of the ceramsite; V_0 represented the volume (mL) of the container.

$$\rho_{bd} = \frac{m}{(V_2 - V_1)} \times 1000 \qquad (2)$$

Where, V_1 and V_2 were volumes (mL) of the ceramic sample before and after the water immersion test.

(2) Water absorption

$$W_{1h} = \frac{(m_1 - m)}{m} \times 100\% \qquad (3)$$

Where, m_1 represented the mass (g) of the ceramsite after the water immersion test.

(3) Bloating index

To evaluate the bloating index of ceramsite (Qi et al., 2009), a uniformly mixed raw material powder was filled into a 12 mm square green body, and the volume change rate of the sample before and after the sintering process was measured and the bloating index (BI) was expressed as the following formula:

$$BI = \frac{(V_4 - V_3)}{V_3} \times 100\% \qquad (4)$$

Where, V_3 represented the volume (mm³) of the dried sample; V_4 represented the volume (mm³) of the sintered ceramic sample.

TABLE 2 Results of orthogonal experiments.

Sample	ODCPRs content (%)	Preheating temperature (°C)	Preheating time (min)	Sintering temperature (°C)	Sintering time (min)	Bulk density (kg/m³)	Standard deviation (kg/m³)	Particle compressive strength (MPa)	Standard deviation (MPa)	1 h water absorption (%)	Standard deviation (%)
$A_1B_1C_1D_1E_1$	A_1	B_1	C_1	D_1	E_1	863.33	6.00	7.66	1.81	17.39	0.96
$A_1B_2C_2D_2E_2$	A_1	B_2	C_2	D_2	E_2	859.17	5.89	10.10	1.52	6.74	0.95
$A_1B_3C_3D_3E_3$	A_1	B_3	C_3	D_3	E_3	446.67	6.60	4.01	1.16	1.78	0.19
$A_1B_4C_4D_4E_4$	A_1	B_4	C_4	D_4	E_4	297.67	2.62	1.96	0.52	4.77	1.65
$A_2B_1C_2D_3E_4$	A_2	B_1	C_2	D_3	E_4	478.33	3.09	2.58	0.73	2.18	0.48
$A_2B_2C_1D_4E_3$	A_2	B_2	C_1	D_4	E_3	355.50	1.50	1.88	0.41	2.77	0.72
$A_2B_3C_4D_1E_2$	A_2	B_3	C_4	D_1	E_2	893.33	4.11	9.00	1.09	15.39	0.10
$A_2B_4C_3D_2E_1$	A_2	B_4	C_3	D_2	E_1	952.00	19.25	10.12	1.69	4.78	0.68
$A_3B_1C_3D_4E_2$	A_3	B_1	C_3	D_4	E_2	460.00	5.72	2.94	0.55	2.62	0.46
$A_3B_2C_4D_3E_1$	A_3	B_2	C_4	D_3	E_1	587.92	1.56	5.41	0.89	2.92	0.46
$A_3B_3C_1D_2E_4$	A_3	B_3	C_1	D_2	E_4	770.56	6.85	9.32	1.68	1.90	0.17
$A_3B_4C_2D_1E_3$	A_3	B_4	C_2	D_1	E_3	1018.67	10.37	11.59	1.90	9.03	1.20
$A_4B_1C_4D_2E_3$	A_4	B_1	C_4	D_2	E_3	755.00	8.92	8.14	1.88	2.20	0.12
$A_4B_2C_3D_1E_4$	A_4	B_2	C_3	D_1	E_4	980.00	19.80	10.35	2.43	4.92	0.35
$A_4B_3C_2D_4E_1$	A_4	B_3	C_2	D_4	E_1	504.00	4.55	2.94	0.26	2.54	0.76
$A_4B_4C_1D_3E_2$	A_4	B_4	C_1	D_3	E_2	501.00	2.00	3.23	0.17	1.93	0.08

TABLE 3 Range analysis of orthogonal experiments.

Items	Factors	Average				R	Rank of influence
		P1	P2	P3	P4		
Particle compressive strength (MPa)	A	5.93	5.90	7.32	6.16	1.38	3
	B	5.33	6.94	6.32	6.72	1.61	2
	C	5.52	6.80	6.86	6.13	1.33	4
	D	9.65	9.42	3.81	2.43	7.22	1
	E	6.53	6.32	6.41	6.05	0.48	5
Bulk density (kg/m³)	A	616.71	669.79	709.29	685.00	92.58	3
	B	639.17	695.65	653.64	692.34	3.31	5
	C	622.60	715.04	709.67	633.48	92.45	4
	D	938.83	834.18	503.48	404.29	534.54	1
	E	726.81	678.38	643.96	631.64	95.17	2
1 h water absorption (%)	A	7.67	6.28	4.12	2.90	4.77	3
	B	6.10	4.34	5.40	5.13	1.76	5
	C	6.00	5.12	3.53	6.32	2.80	4
	D	11.68	3.91	2.20	3.18	9.48	1
	E	6.91	6.67	3.95	3.44	3.46	2

2.3.2 Mechanical property

In this paper, the compressive strength of the ceramsite was evaluated using the single-particle strength method (Yashima et al., 1987; Li et al., 2000). Each series was tested with 15 samples by a press machine (ETM305D, Shenzhen Wance Test Equipment Co., Ltd.). The particle compressive strength of ceramsites was calculated as below:

$$S = \frac{2.8 P_c}{\pi X^2} \qquad (5)$$

Here, S was the compressive strength of the ceramsite (MPa); P_c was the failure load of the ceramsite (N); X was the distance between the upper and lower compression plates (mm).

2.3.3 Mineral and chemical composition

The phase composition of the ceramsite was also analyzed using an X-ray diffractometer (XRD, X'Pert PRO MPD, PANalytical, Netherlands), with Cu-Kα radiation (40 Kv, 40 mA, scanning range: 5°–90°, scanning time: 5°/min), and the Inorganic Crystal Structure Database (ICSD) database was used to identify the crystalline phases. Furthermore, the chemical compositions of raw materials were characterized by X-ray fluorescence (XRF, RIGAKU ZSX Priums, Japan).

2.3.4 Thermal properties

The mass changes and thermal behaviors of each raw material and green body were characterized using a thermogravimetric analyzer and differential scanning calorimeter (STA449F3, Netzsch, Germany) with a heating rate of 10°C/min under air atmosphere, and the test temperature range was from room temperature to 1300°C.

2.3.5 Morphological properties

The cross-sectional morphology of the ceramsite before and after acid treatment was observed using a scanning electron microscope (Zeiss Gemini 300, Carl Zeiss, Germany), and their elemental compositions were further determined using energy-dispersive X-ray spectroscopy (EDX). The acid treatment was referred to the Chinese standard "SY/T 5108-2014." The acid solution was first pre-fabricated as HCl: HF = 12: 3 (mass 12% HCl and mass 3% HF). Afterward, the ceramsite sample was immersed in the acid solution and then placed in a thermostatic water bath (CF-B, Cangchuan Road Test Apparatus Co., Ltd.) at a constant temperature of 66°C for 3 h to remove the soluble substances from the ceramsite.

2.3.6 Chemical properties

The heavy metals leaching behavior of ceramsites was evaluated by the sulfuric-nitric acid method which was referred to the "Solid Waste-Extraction Procedure for Leaching Toxicity" (HJ/T 299-2007).

3 Results and discussion

3.1 Optimization of sintering parameters

In this study, an orthogonal experiment was designed to investigate the optimal content of drilling cuttings and the sintering conditions for the preparation of ceramsites. The experiment included five influencing factors: A) ODCPRs contents, B) preheating temperature, C) preheating time, D) sintering temperature, and E) sintering time. At the same
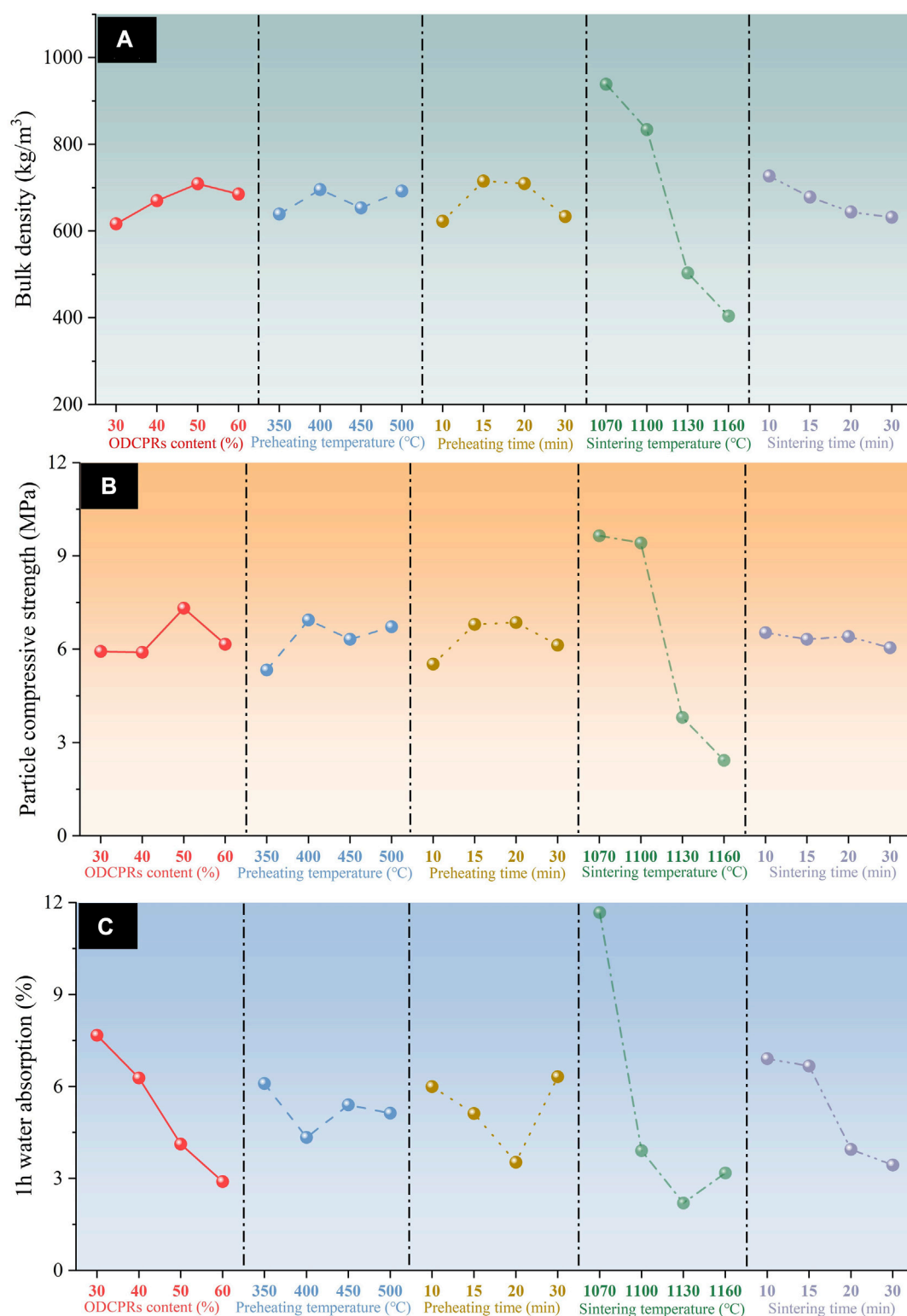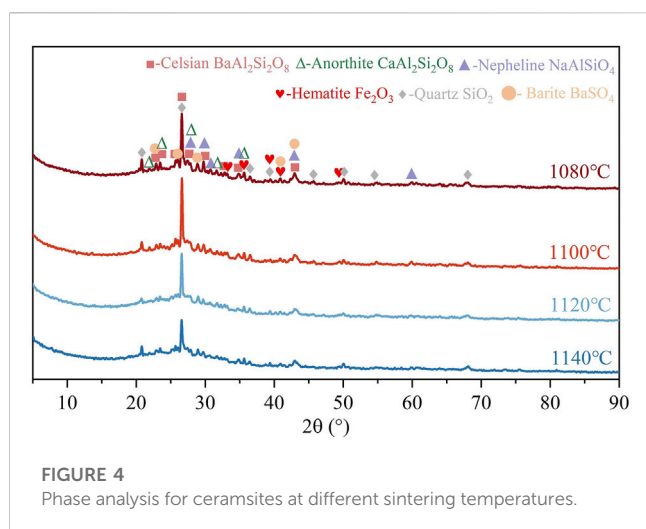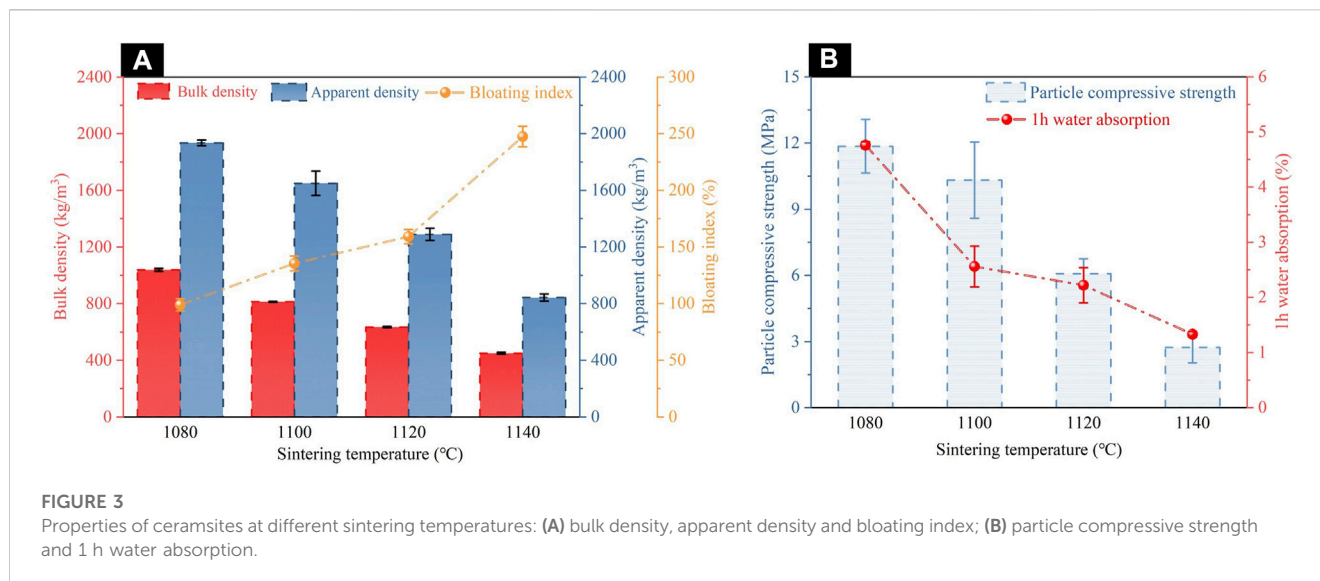
FIGURE 2
Influences of ODCPRs content, preheating temperature, preheating time, sintering temperature, and sintering time on **(A)** bulk density, **(B)** particle compressive strength, and **(C)** 1 h water absorption.

time, four-level factors were also settled. In addition, the heating rate was controlled at 10°C/min, the detail of the sintering parameters was shown in Table 1. The bulk density, particle compressive strength, and 1 h water absorption of ceramsites under different orthogonal experimental conditions were analyzed.

FIGURE 3
Properties of ceramsites at different sintering temperatures: **(A)** bulk density, apparent density and bloating index; **(B)** particle compressive strength and 1 h water absorption.

FIGURE 4
Phase analysis for ceramsites at different sintering temperatures.

The results of the orthogonal test were shown in Table 2, a total of 16 groups of ceramsites have been tested. Thereinto, sample $A_2B_4C_4D_4E_4$ has the lowest bulk density of 297.67 kg/m³, but the strength was only 1.95 MPa. Besides, sample $A_3B_4C_2D_1E_3$ presented the highest strength of 11.59 MPa, while the bulk density was 1018.67 kg/m³, the density was higher than the maximum value of lightweight requirements of the standard. Hence, it was difficult to decide the optimum conditions for preparing ceramsite. In order to comprehensively analyze the test results and find out the primary factors impacting the performance of the ceramsite, the range analysis of orthogonal experiment was employed, as shown in Table 3. As presented in Table 3, Pi value represented the average value of the experimental results under the same factor level, while R value represented the difference between the maximum and minimum Pi values under the same factor, indicating the degree of dispersion of the experimental data. The larger the R value, the greater the impact of this factor on the properties of the ceramsites was obtained, indicating that this factor was the main factor. Hence, it can be concluded that sintering temperature was the most important factor affecting the ceramsite properties of compressive strength, followed by bulk density, and 1 h water absorption.

Furthermore, as shown in Figure 2, the bulk density and particle compressive strength of ceramsites decreased with the increase in sintering temperature, while the water absorption rate first decreased and then increased. At a sintering temperature of 1070°C, insufficient sintering reaction resulted in inadequate generation of both liquid and gas phases, leading to an average water absorption rate exceeding 10% for the ceramsites at this level. Additionally, the higher density failed to meet the requirement for lightweight materials. With an increase in sintering temperature, more liquid phase, and gas phase would be generated inside the ceramsites, promoting the formation of higher porosity and resulting in a reduction in bulk density and compressive strength (Zhuo et al., 2023). Meanwhile, the formation of a sufficient liquid phase resulted in the development of a glassy layer on the surface, effectively reducing water absorption by the ceramsite.

A significant impact of the ODCPRs content on the properties of ceramsites was observed through comparison. As the ODCPRs content increased, both the bulk density and particle compressive strength showed a trend of first increasing and then decreasing. This may be related to the balance between high-temperature melt components and gas components in the green body (Jia et al., 2023). When the ODCPRs content was low, the gas cannot be wrapped and was affected by the low liquid content in the ceramsite, leading to an outward overflow of gas and resulting in an excessively high density of the ceramsite (Zhuo et al., 2023). Gradually, with an increase in ODCPRs content, the sufficient liquid phase was generated inside the body, and gas accumulated within the ceramsites to promote liquid-phase expansion (Jia et al., 2023). This resulted in the formation of numerous internal pores, ultimately leading to a decrease in both bulk density and particle compressive strength (Zhuo et al., 2023).

As indicated by Table 3, the impact of preheating temperature had little influence on the compressive strength of the ceramic particles, meanwhile the preheating temperature was number 5 in
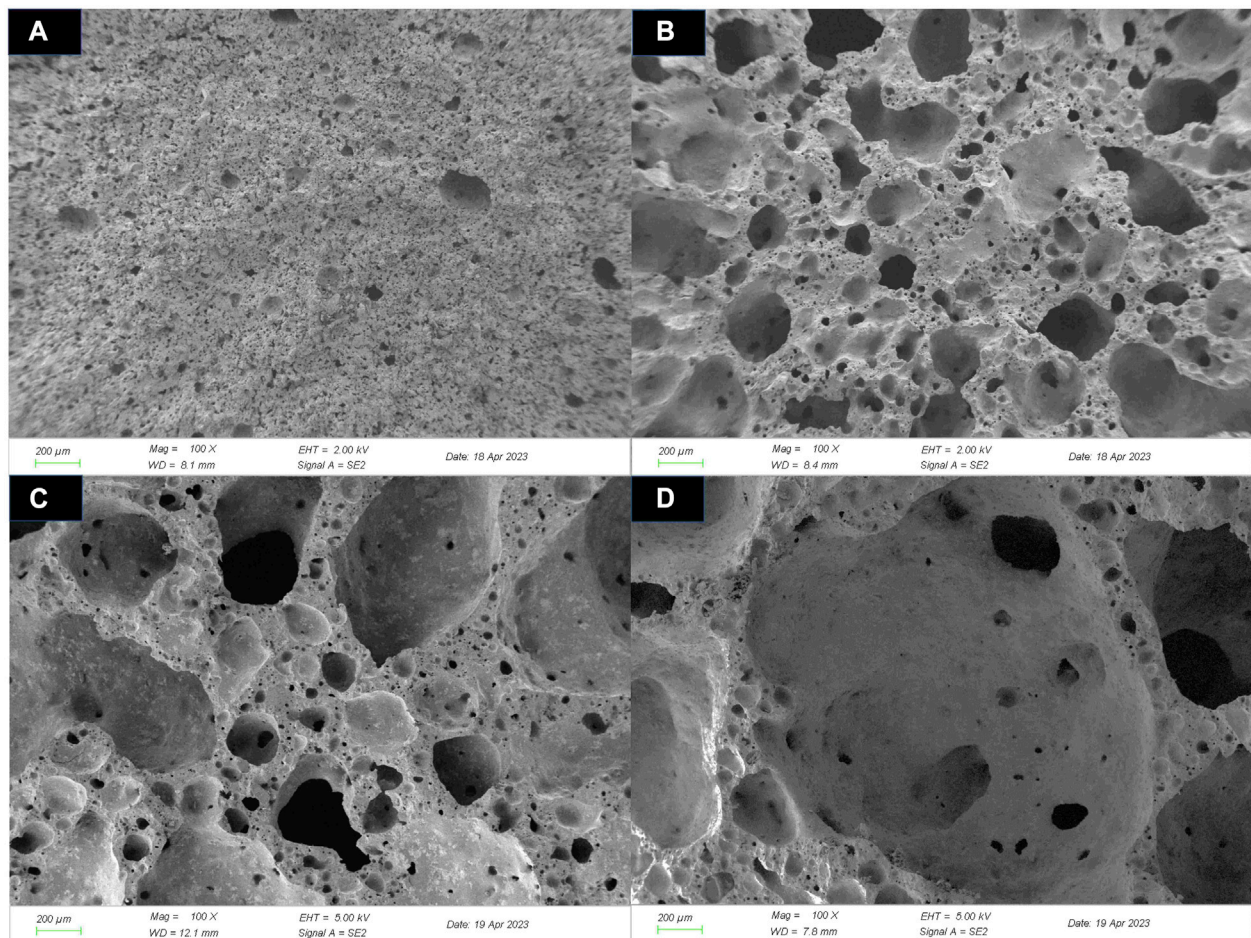
FIGURE 5
Microstructure (×100) of ceramsites before acid treatment at different sintering temperatures: **(A)** 1,080°C, **(B)** 1,100°C, **(C)** 1,120°C, and **(D)** 1,140°C.

the ranking on the bulk density and 1 h water absorption. Therefore, among the five factors, the preheating temperature was found to be negligible on the performance of ceramsites. But preheating served to remove water from the green body of the ceramsite to prevent cracking during the sintering process and to regulate gas release during the sintering stage. When the preheating process happened at rather lower temperatures, pores could be filled by the liquid phase generated at higher temperatures. Therefore, the preheating temperature displayed minimal influences on bulk density, particle compressive strength, and 1 h water absorption.

Besides, the optimal factor was determined based on the principle of achieving a ceramsite with enhanced strength, reduced density, and minimized water absorption while taking into account the consumption of cuttings and energy efficiency during preparation. The optimal sintering conditions were determined as follows: with an ODCPRs content of 50%, preheating-temperature-of 400°C for 20 min, the sintering temperature of 1100°C for 10 min, and heating rate of 10°C/min. Under these optimal sintering conditions, the ceramsites exhibited excellent properties, including a bulk density of 813.00 kg/m^3, a particle compressive strength of 10.31 MPa, and water absorption of 2.56%.

3.2 Influence of sintering temperature on properties of ceramsites

Formulation S3 was selected as the test sample for investigating the impact of sintering temperature and heating rate on the properties of ceramsites containing 50% ODCPRs content.

3.2.1 Physical properties of ceramsites

Based on the orthogonal experiment results determined in Section 3.1, the optimal sintering conditions for ceramsites were established. Besides, it was found that sintering temperature had the greatest impact on the properties of ceramsites, with a wide range of temperature variations. Therefore, the range of sintering temperatures based on the optimal conditions from the orthogonal experiments was further investigated using a single-factor method, and formulation S3 was chosen for the further experiment.

Figure 3 presented the changes in properties of ceramsites at different sintering temperatures. It was observed that the ceramsites were highly sensitive to the sintering temperature. As the sintering temperature increased, the bulk density, apparent density, particle compressive strength, and water absorption of the ceramsites were
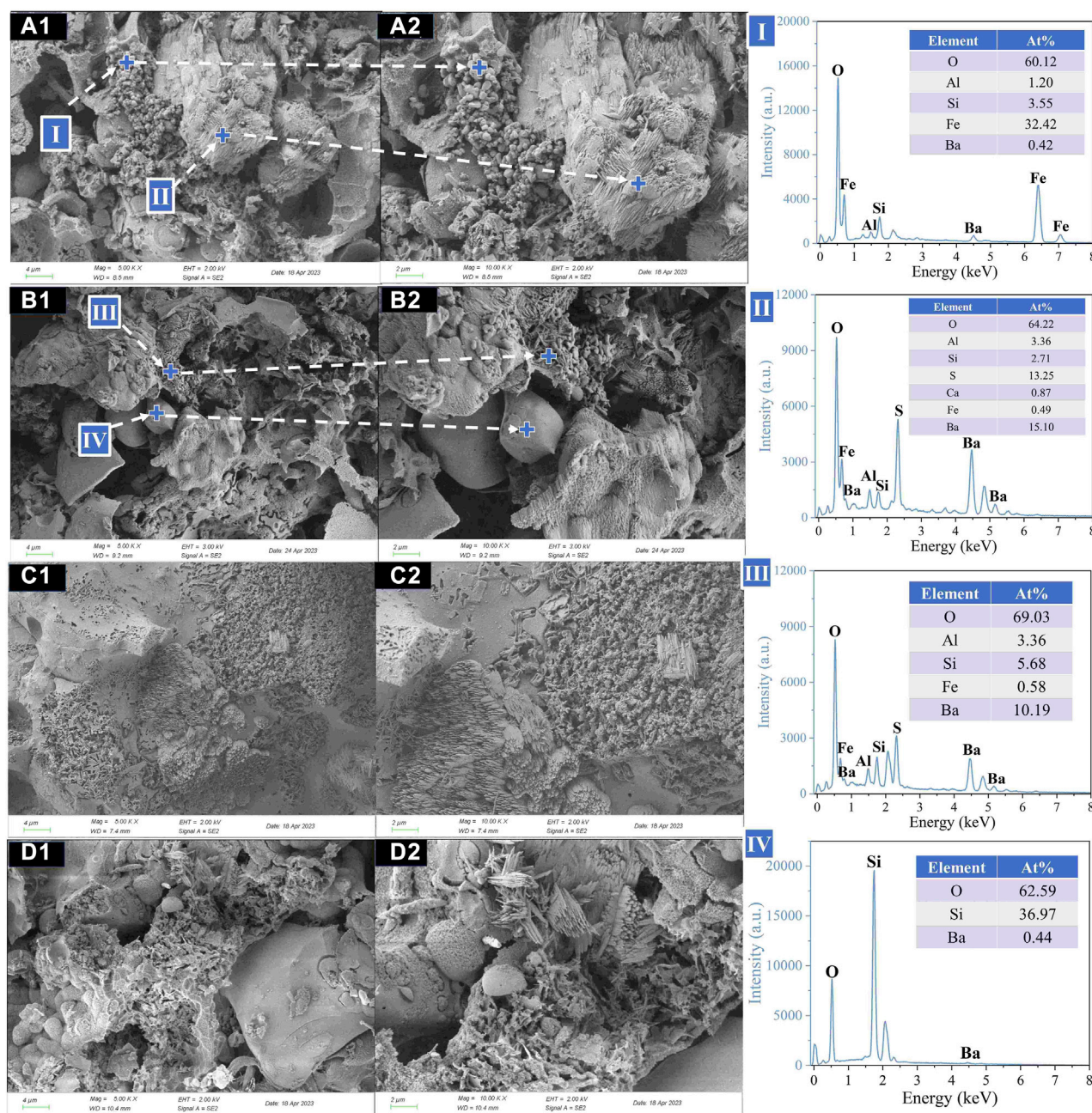
FIGURE 6
Microstructure (×5,000, ×10,000) of ceramsites after acid treatment at different sintering temperatures: **(A)** 1,080°C; **(B)** 1,100°C; **(C)** 1,120°C; **(D)** 1,140°C.

all decreased. The bloating index showed a negative correlation with these factors, which was in accordance with the results of the orthogonal experiment. When a sintering temperature was set at 1080°C, the compressive strength of the ceramsites reached 11.85 MPa, but the bulk density and apparent density were also increased to 1038.33 and 1934.83 kg/m³, respectively, indicating poor foaming and swelling effects at lower sintering temperatures. Additionally, at lower sintering temperatures, the mass transfer process of the liquid phase was limited, which could lead to a thinner glassy layer formed on the surface of the ceramsites, more interconnected pores and micro-pores in the

interior, and higher water absorption (4.76%) would occur. In contrast, when the sintering temperature increased to 1140°C, the liquid phase content in the green body increased, and the mass transfer process of the liquid phase intensified. A denser shell formed on the surface of the ceramsites, blocking the interconnected pores inside and effectively preventing water from infiltrating, resulting in reduced water absorption of 1.33%. Moreover, the increased liquid phase contributed to encapsulating the gas generated by high-temperature reactions and facilitating the formation of a closed porous structure. This manifested as a continuous decrease in the bulk density and
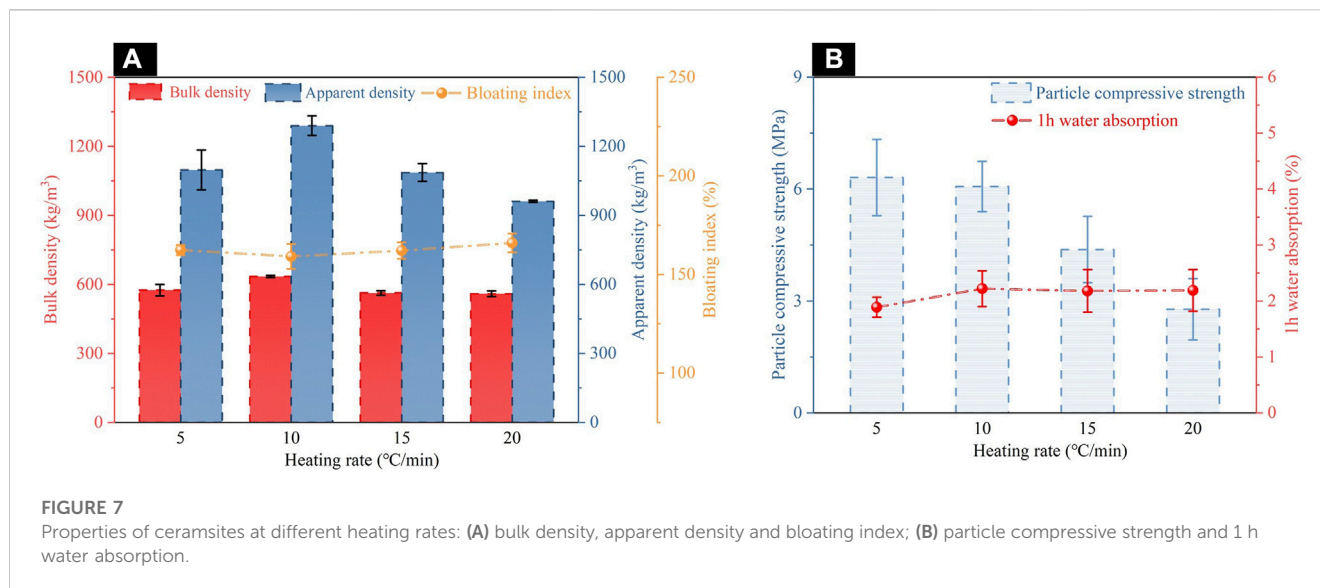
FIGURE 7
Properties of ceramsites at different heating rates: **(A)** bulk density, apparent density and bloating index; **(B)** particle compressive strength and 1 h water absorption.
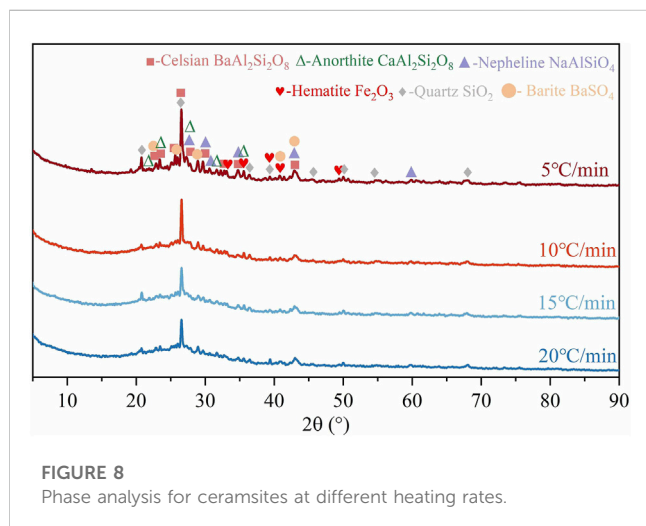

FIGURE 8
Phase analysis for ceramsites at different heating rates.

pores, induce sliding, rotation, re-arrangement of the internal fine particles, and accelerate solid-solid and solid-liquid reactions, thereby promoting crystal formation (Yoon et al., 2003; Shih and Jean, 2017; Yang et al., 2018). From the XRD spectra, it could be observed that as the sintering temperature increased from 1080°C to 1140°C, the diffraction peak intensity of celsian first increased and then decreased, reaching the maximum intensity at 1100°C, indicating that a suitable liquid-phase content for foaming and sintering reactions could be achieved at this sintering temperature. However, with further increase in sintering temperature, the peak intensities of all crystals significantly decreased due to excessive formation of glass phase and larger internal porosity. These factors may potentially have adverse effects on the properties of the ceramsite (Ren et al., 2019).

3.2.3 Morphological analysis

Figure 5 showed the cross-sectional pictures of ceramsites at different sintering temperatures. It can be clearly observed that as the sintering temperature increased, the internal pores of the ceramsites became significantly larger. This was caused by the gradual increase of liquid phases and the decline of liquid phases viscosity during the sintering process. In this stage, the gas-producing components in the ceramsite would be released to generate a large amount of gas. When sufficient liquid phases were formed, the gas could be easier encapsulated by the liquid phase, thus forcing the matrix to expand and creating numerous pores inside the ceramsite (Jun et al., 2023). However, at excessively high sintering temperatures, the viscosity of the liquid phase decreased, which facilitated the migration and diffusion of gas phases, which resulted in the merging and enlargement of small enclosed pores to form larger ones, or even causing the gas escape. This was the main reason for the decrease in density and strength of the ceramsite.

Figure 6 displayed the microstructure of the ceramsite after acid corrosion treatment. Combined with the EDS test (II, III), it could be inferred that celsian ($BaAl_2Si_2O_8$) mainly appeared in the form of clusters or needles. In addition, a large amount of sulfur element was detected ascribed to the EDS results, indicating that the formation of celsian crystals was due to the solid-phase reaction between barite ($BaSO_4$), quartz (SiO_2), and Al_2O_3 in the matrix (Long-González et al.,

apparent density of the ceramsites. In summary, when the sintering temperature was set at 1120°C, the ceramsites exhibited optimal properties: a bloating index of 159.15%, particle compressive strength of 6.07 MPa, bulk density of 634 kg/m³, apparent density of 1289.34 kg/m³, and water absorption of 2.22%.

3.2.2 Phase analysis

The X-ray diffraction (XRD) spectra of the ceramsite samples at different sintering temperatures were shown in Figure 4. It was observed that the sample compositions were similar at different sintering temperatures, the main crystal phases consisted of celsian, quartz, hematite, anorthite, barite, and nepheline. Thereinto, celsian was the main crystalline phase of sintering ceramsite, while unreacted barite, quartz, and hematite still remained. Moreover, the generation of celsian crystals was closely related to the sintering temperature and liquid-phase content in the ceramsite. The generation of adequate liquid-phase production could reduce the activation energy for ion diffusion, immerse the internal fine particles of the ceramsite, enhance capillary forces between particles, promote liquid flow between
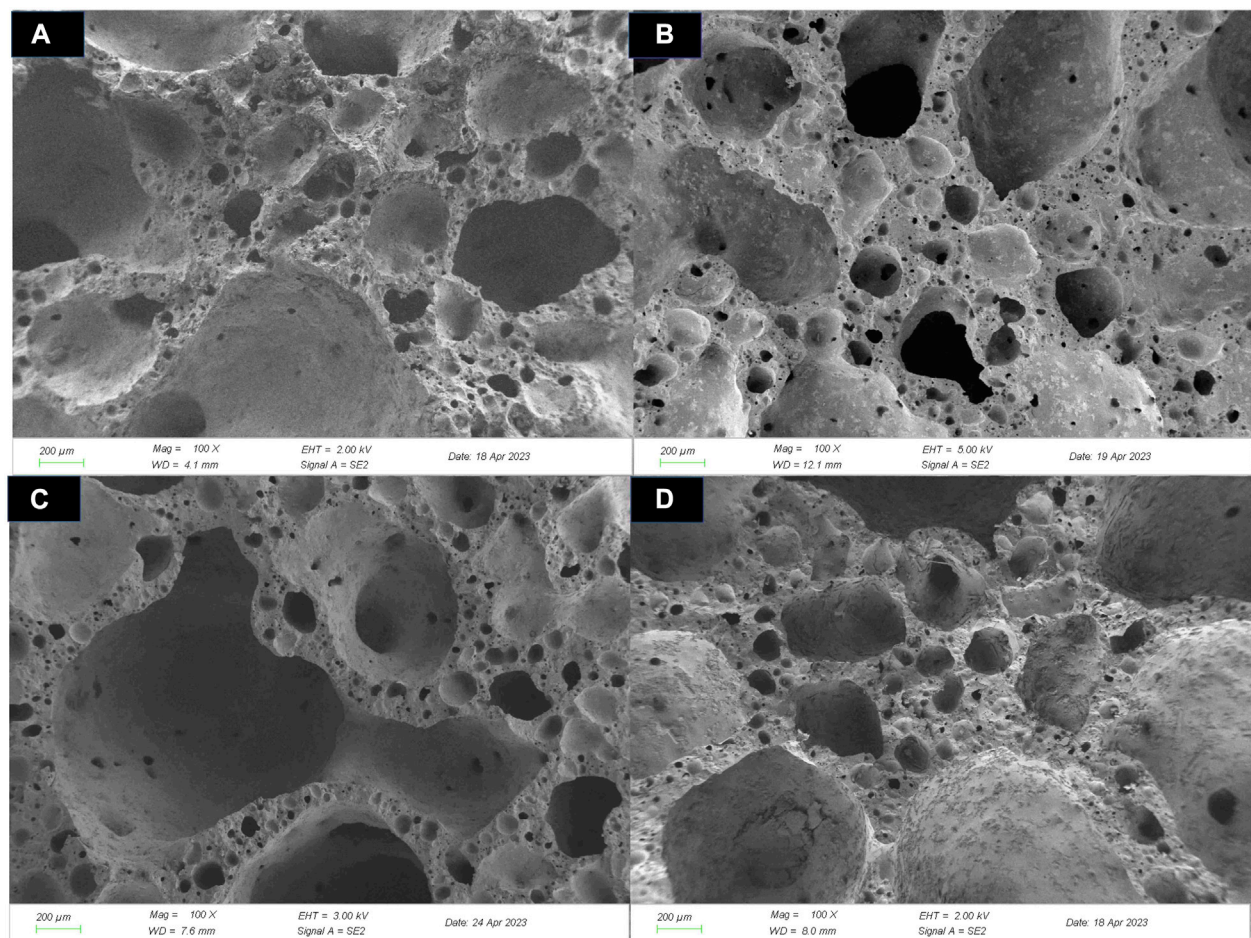
FIGURE 9
Microstructure (×100) of ceramsites before acid treatment at different heating rates: **(A)** 5°C/min; **(B)** 10°C/min; **(C)** 15°C/min; **(D)** 20°C/min.

2009; Yang et al., 2018). According to the EDS result (I), it was deduced that unreacted hematite (Fe_2O_3) mainly existed in the form of particles. According to the EDS result (IV), the blocky particles were unreacted quartz. At a lower sintering temperature (1080°C), a large amount of unreacted hematite was found, and the celsian phases mainly showed a cluster structure. However, when the sintering temperature increased to 1100°C, needle-shaped celsian gradually appeared and overlapped with each other to form a denser structure, thereby improving the mechanical properties of the ceramsite. Meanwhile, a notable augmentation in the internal porosity of the ceramsite was observed. As the sintering temperature gradually increased to 1140°C, there was a gradual reduction in the number of celsian crystal clusters but an increase in their size (as depicted in Figure 6D). Concurrently, it was discovered that the internal porosity of the ceramsite underwent significant expansion.

3.3 Influence of heating rate on properties of ceramsites

3.3.1 Physical properties of ceramsites

Through the single factor method study of the sintering temperature, the following ceramsites calcination conditions were

determined: ODCPRs content of 50% for formulation S3, the preheating temperature of 400°C for 20 min, the sintering temperature of 1120°C for 10 min. In this section, the influence of heating rate (5°C/min, 10°C/min, 15°C/min, and 20°C/min) on the properties of the ceramsite was further investigated, as shown in Figure 7. It was found that the variation in heating rate had little influence on the water absorption of the ceramsite. The bulk density and apparent density both showed an upward trend followed by a downward trend, while the bloating index exhibited the opposite trend. This may be attributed to the slower rate of substance decomposition or gas generation during the reaction, compared to that of molten liquid phase formation, when the heating rate was ≤10°C/min, resulting in impeded pore formation. When the heating rate continued to increase, the decomposition reaction became more intense, and the generated gas was sufficient to form relatively large pores on the surface of the matrix, leading to a relatively lower bulk density and apparent density. Moreover, the particle compressive strength of the ceramsite decreased with the increase of the heating rate, especially at a heating rate of 20°C/min, where its particle compressive strength was only 2.78 MPa. In summary, when the heating rate was 5°C/min, the physical properties of the ceramsite were finest, with bulk density, apparent density, 1 h water absorption, particle compressive
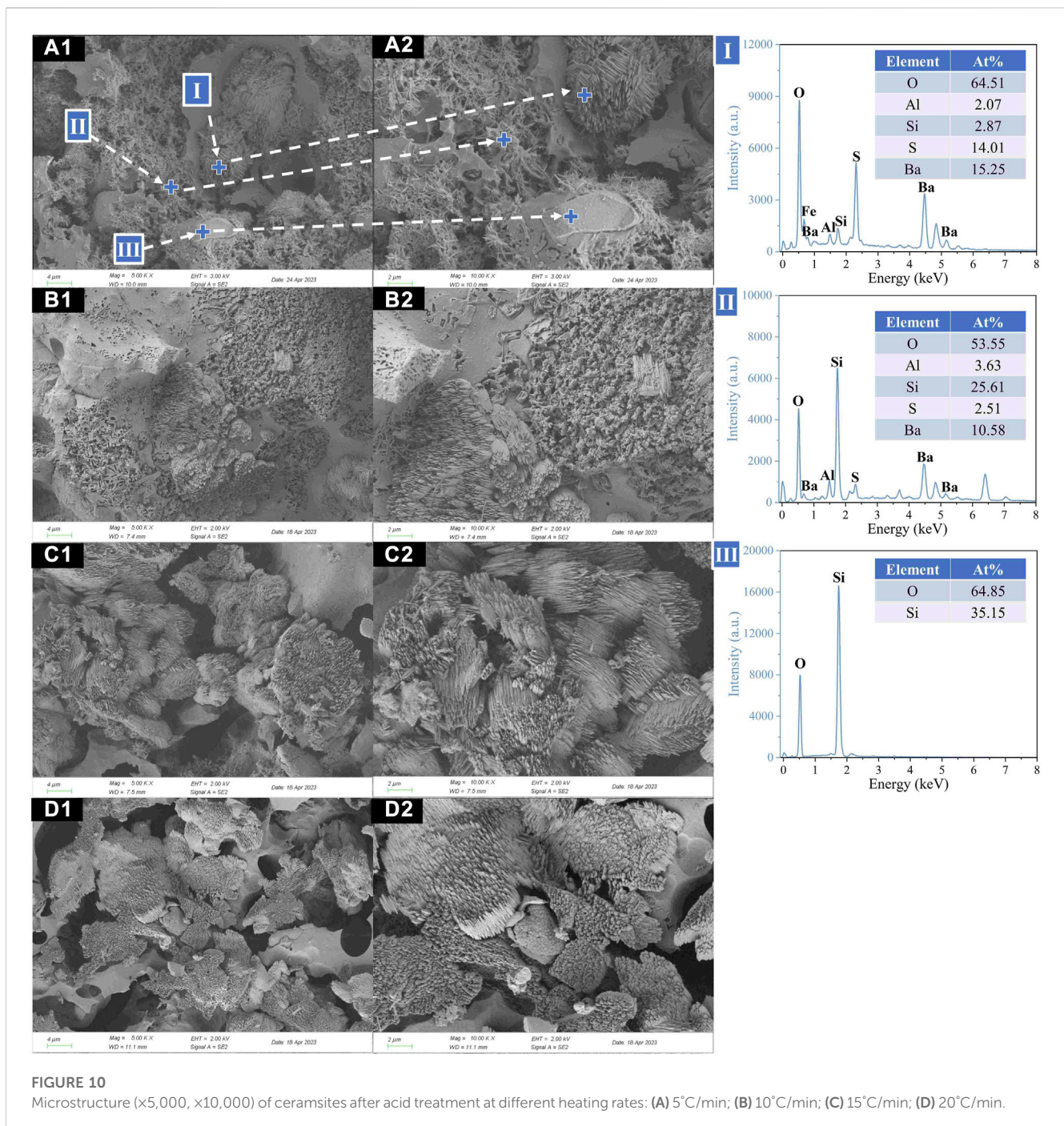
FIGURE 10
Microstructure (×5,000, ×10,000) of ceramsites after acid treatment at different heating rates: **(A)** 5°C/min; **(B)** 10°C/min; **(C)** 15°C/min; **(D)** 20°C/min.

strength, and bloating index reaching 575.11 kg/m³, 1097.24 kg/m³, 1.89%, 6.31 MPa, and 162.38%, respectively.

3.3.2 Phase analysis

The XRD spectra of ceramsites were presented in Figure 8, showing the results of phase compositions at different heating rates. The experimental results showed that with the increase in heating rate, the diffraction peak intensity of each crystal decreased significantly. When the heating rate of the sintering process was 5°C/min, the diffraction peak intensity of crystals such as celsian, quartz, anorthite, and nepheline increased significantly compared to the sample sintered in 10°C/min. This was attributed to the

prolonged residence time of the matrix in the high-temperature stage at a heating rate of 5°C/min, which facilitated phase reactions and resulted in an increased formation of highly crystalline crystals. However, when the heating rate exceeded 10°C/min, the particle's residence time at high temperature continuously decreased, leading to insufficient phase reaction and a significant reduction in both diffraction peak intensity and compressive strength of the ceramsite particles.

3.3.3 Morphological analysis

Figure 9 showed the cross-sectional microstructure of ceramsites under different heating rates. It was observed that as the heating rate
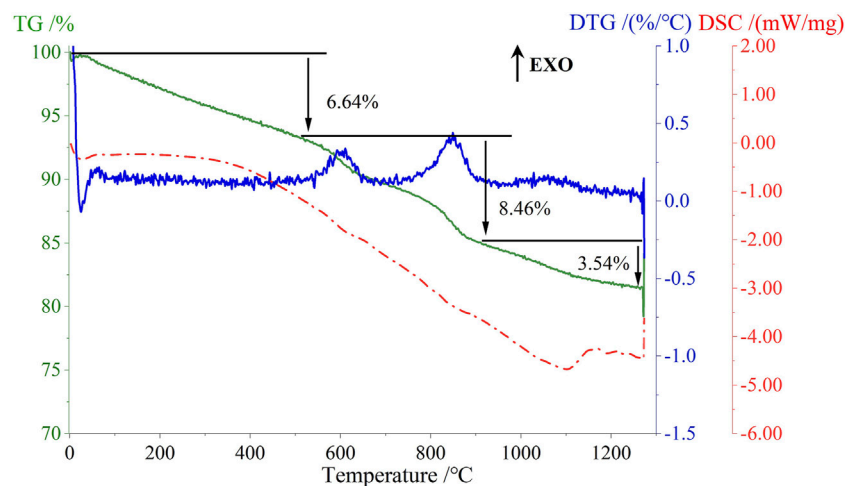
FIGURE 11
Sample S3 TG-DSC curves.

TABLE 4 Heavy metal leaching results of the ceramsites (mg/L).

Elements	Cr	Ba	Ni	Zn	Cd	Hg	Cu	Pb
Expanded clay aggregates	1.02	0.78	0.07	1.33	ND	0.00008	ND	ND
Limits specified in "GB 5085.3–2007"	15	100	5	100	1	0.1	100	5

increased, the size of internal pores within the ceramsite exhibited a first-increasing-then-decreasing trend, which was consistent with the density variation pattern of ceramsites discussed in Section 3.3.1. While Figure 10 showed the cross-sectional microstructure of ceramsites after the acid treatment under different heating rates. It was found that when the heating rate was 5°C/min, celsian still mainly appeared in the form of interactive overlapping with needle-shaped or cluster crystals. As the EDS results (I, II) revealed that unreacted quartz particles and barite crystals appeared around the celsian crystals. Furthermore, it was noticed that with the increase in heating rate, the celsian in the green body tended to transform from a needle-shaped structure into a cluster structure, indicating the influence of the heating rate on the morphology change of celsian crystals.

3.4 TG-DSC analysis

In order to clarify the sintering behavior and phase reaction mechanism during the ceramsites sintering procedure, TG-DSC experimental analyses were conducted on the formulation S3, as shown in Figure 11.

As shown in Figure 11, the TG curve of the sample S3 exhibited a similar overall trend to that of the ODCPRs, which was with three weight loss stages observed at different temperature ranges: "room temperature to 550°C," "550°C–900°C," and "900°C–1300°C," which were corresponding to the loss of moisture and combustion of organic compounds (6.46%), the decomposition of carbonates and the loss of bound water in boehmite (8.46%), and the

decomposition of hematite and sulfates (3.54%), respectively. These observations indicated that gas-phase decomposition occurred during the entire sintering process, contributing to the reduction in the density of the ceramsite. Additionally, the DSC curve continued to decrease from 500°C, indicating that the process was continuously endothermic, which was related to the endothermic decomposition of carbonates, sulfates, and the oxidation reaction of SiC. Moreover, a distinctive endothermic peak appeared at 1104°C, corresponding to the occurrence of solid-state reactions at high temperatures. Compared with the endothermic peak of ODCPRs appearing at 1065°C, this peak was slightly delayed due to the introduction of fly ash and quartz sand with higher alumina-silica content, leading to a decrease in the liquid phase generation at high temperatures, thereby delaying the solid-phase reaction temperature range. Combining with the XRD analysis results that were discussed earlier, it was known that the main solid-phase reactions in this temperature range were the formation of celsian crystals (Long-González et al., 2009) and wollastonite crystals (Guzmán-Carrillo et al., 2017), involving the following chemical reaction equations in Supplementary Table S3.

3.5 Analysis of heavy metals leaching behavior in ceramsites

The major raw material used in this study for the preparation the ceramsites was ODCPRs, which may still face some trace amounts of environmentally harmful substances. If these recycling products released heavy metal ions during the application, they would pose a

threat to the natural environment and human beings. Therefore, it was important to evaluate the stabilization effect of ceramsites on heavy metal ions after the sintering process and their environmental safety during application. According to the Chinese standard "GB 5085.3-2007," the heavy metal leaching concentration of sample S3's ceramsites was tested under optimal preparation conditions, as presented in Table 4. The experimental results showed that after high-temperature sintering, the heavy metal leaching concentrations of the ceramsites were much lower than the national standard limits indicating a good environmental safey of the ceramsite.

The comparison of the bulk density, water absorption, and particle compressive strength of the ceramsite in this study with those reported in other literature was presented in Supplementary Table S4 (Sun et al., 2021; Pei et al., 2022; Shang et al., 2022; Jia et al., 2023; Li et al., 2023). It was worth noting that all primary raw materials utilized were industrial solid waste materials, and the produced ceramsite in this work demonstrated exceptional performance in terms of both compressive strength and density.

4 Conclusion

This study demonstrated the feasibility of using ODCPRs in combination with solid waste for the preparation ceramsites. The properties of the ceramsite were comprehensively investigated through orthogonal experiments, single-factor analysis, phase, morphological, and TG-DSC analysis, the following conclusions were drawn:

(1) By optimizing the sintering parameters, it was determined that the sintering temperature exerted the most significant influence on the properties of ceramsites. The order of impact on the particle compressive strength of ceramsites was found to be as follows: sintering temperature > ODCPRs content > sintering time > preheating time > preheating temperature.

(2) The independent influence of sintering temperature and heating rate on the properties of ceramsites was explored by a single-factor method. By combining XRD and SEM analysis, the phase composition and microstructure changes of the ceramsite were revealed. The results indicated that the physical properties of the ceramsite decreased with increasing sintering temperature, while reducing the heating rate was conducive to improving the particle compressive strength. Furthermore, the main crystal phases of the ceramsites were identified as celsian, quartz, hematite, zircon, and xenotime, and the best preparation process parameters were obtained as: "preheating temperature of 400°C for 20 min, sintering temperature of 1120°C for 10 min with a heating rate of 5°C/min and 50% content of ODCPRs". The bulk density, apparent density, particle compressive strength, 1 h water absorption, and bloating index of the obtained ceramsites were 575.11 kg/m³, 1097.24 kg/m³, 6.31 MPa, 1.89%, and 162.38%, respectively.

(3) During high-temperature sintering, various gas-phase and solid-phase reactions occurred in the matrix, including water vapor vaporization, organic matter combustion, as well as carbonates, sulfates and hematite decomposition. These reactions contributed to the expansion and density reduction of ceramsites.

(4) The sintered ceramsites could well meet the Chinese standards of "GB 5985.3-2007" for the leaching toxicity of heavy metals.

Data availability statement

The original contributions presented in the study are included in the article/Supplementary Material, further inquiries can be directed to the corresponding author.

Author contributions

HW, YY, and JL contributed to conception and design of the study. HL and TM organized the database. JY and LZ performed the statistical analysis. YY and HW wrote the first draft of the manuscript. DL, GJ, and HL wrote portion sections of the manuscript. All authors contributed to the article and approved the submitted version.

Conflict of interest

Authors HW, JL, DL, GJ, LZ, JY, TM, and XH were employed by Safety and Technology Supervision Research Institute of PetroChina Southwest Oil and Gas Field Company.

The remaining authors declare that the research was conducted in the absence of any commercial or financial relationships that could be construed as a potential conflict of interest.

Publisher's note

All claims expressed in this article are solely those of the authors and do not necessarily represent those of their affiliated organizations, or those of the publisher, the editors and the reviewers. Any product that may be evaluated in this article, or claim that may be made by its manufacturer, is not guaranteed or endorsed by the publisher.

Supplementary material

The Supplementary Material for this article can be found online at: https://www.frontiersin.org/articles/10.3389/fmats.2023.1245121/full#supplementary-material

References

Abbe, O. E., Grimes, S. M., Fowler, G. D., and Boccaccini, A. R. (2009). Novel sintered glass-ceramics from vitrified oil well drill cuttings. *J. Mat. Sci.* 44, 4296–4302. doi:10.1007/s10853-009-3637-y

Abnisa, F., and Alaba, P. A. (2021). Recovery of liquid fuel from fossil-based solid wastes via pyrolysis technique: a review. *J. Environ. Chem. Eng.* 9, 106593. doi:10.1016/j.jece.2021.106593

Ahmad, M. R., and Chen, B. (2019). Experimental research on the performance of lightweight concrete containing foam and expanded clay aggregate. *Compos Part B. Eng.* 171, 46–60. doi:10.1016/j.compositesb.2019.04.025

Ball, A. S., Stewart, R. J., and Schliephake, K. (2012). A review of the current options for the treatment and safe disposal of drill cuttings. *Waste. manage. Res.* 30, 457–473. doi:10.1177/0734242x11419892

Başaran Bundur, Z., Kirisits, M. J., and Ferron, R. D. (2017). Use of pre-wetted lightweight fine expanded shale aggregates as internal nutrient reservoirs for microorganisms in bio-mineralized mortar. *Cem. Concr. Comp.* 84, 167–174. doi:10.1016/j.cemconcomp.2017.09.003

Bernardo, G., Marroccoli, M., Nobili, M., Telesca, A., and Valenti, G. L. (2007). The use of oil well-derived drilling waste and electric arc furnace slag as alternative raw materials in clinker production. *Resour. Conserv. Recy.* 52, 95–102. doi:10.1016/j.resconrec.2007.02.004

Chaillan, F., Chaîneau, C. H., Point, V., Saliot, A., and Oudot, J. (2006). Factors inhibiting bioremediation of soil contaminated with weathered oils and drill cuttings. *Environ. Pollut.* 144, 255–265. doi:10.1016/j.envpol.2005.12.016

Du, H., Zhong, Z. P., Zhang, B., Zhao, D. Q., Lai, X. D., Wang, N. B., et al. (2021). Comparative study on intercalation-exfoliation and thermal activation modified kaolin for heavy metals immobilization during high-organic solid waste pyrolysis. *Chemosphere* 280, 130714. doi:10.1016/j.chemosphere.2021.130714

Foroutan, M., Hassan, M., M., Desrosiers, N., and Rupnow, T. (2018). Evaluation of the reuse and recycling of drill cuttings in concrete applications. *Constr. Build. Mat.* 164, 400–409. doi:10.1016/j.conbuildmat.2017.12.180

Guzmán-Carrillo, H. R., Pérez, J. M., and Romero, M. (2017). Crystallisation of nepheline-based glass frits through fast-firing process. *J. Non-Cryst. Solids.* 470, 53–60. doi:10.1016/j.jnoncrysol.2017.04.043

Hao, C. M., Cheng, Y. P., Wang, L., Liu, H. Y., and Shang, Z. (2019). A novel technology for enhancing coalbed methane extraction: hydraulic cavitating assisted fracturing. *J. Nat. Gas. Sci. Eng.* 72, 103040. doi:10.1016/j.jngse.2019.103040

He, H. T., Zhao, P., Yue, Q. Y., Gao, B. Y., Yue, D. T., and Li, Q. (2015). A novel polynary fatty acid/sludge ceramsite composite phase change materials and its applications in building energy conservation. *Renew. Energy* 76, 45–52. doi:10.1016/j.renene.2014.11.001

Ji, T., Zheng, D. D., Chen, X. F., Lin, X. J., and Wu, H. C. (2015). Effect of prewetting degree of ceramsite on the early-age autogenous shrinkage of lightweight aggregate concrete. *Constr. Build. Mat.* 98, 102–111. doi:10.1016/j.conbuildmat.2015.08.102

Jia, G. H., Wang, Y. L., Yang, F. L., and Ma, Z. B. (2023). Preparation of CFB fly ash/sewage sludge ceramsite and the morphological transformation and release properties of sulfur. *Constr. Build. Mat.* 373, 130864. doi:10.1016/j.conbuildmat.2023.130864

Jun, J., Song, C., Chao, J., Gui, W., Tie, L., Xu, T., et al. (2023). Preparation and properties of high-strength lightweight aggregate ceramsite from nepheline tailings. *Constr. Build. Mat.* 368, 130458. doi:10.1016/j.conbuildmat.2023.130458

Khalil, N. M., Algamal, Y., and Saleem, Q. M. (2018). Exploitation of petroleum waste sludge with local bauxite raw material for producing high-quality refractory ceramics. *Ceram. Int.* 44, 18516–18527. doi:10.1016/j.ceramint.2018.07.072

Kingman, S. W., Robinson, J. P., Snape, C. E., Barranco, R., Shang, H., Bradley, M., et al. (2009). Remediation of oil-contaminated drill cuttings using continuous microwave heating. *Chem. Eng. J.* 152, 458–463. doi:10.1016/j.cej.2009.05.008

Lau, P. C., Teo, D. C. L., and Mannan, M. A. (2017). Characteristics of lightweight aggregate produced from lime-treated sewage sludge and palm oil fuel ash. *Constr. Build. Mat.* 152, 558–567. doi:10.1016/j.conbuildmat.2017.07.022

Li, C. B., Zhang, G. F., Liu, D. Z., and Wang, M. T. (2023). Preparation of lightweight ceramsite from solid waste lithium slag and fly ash. *Constr. Build. Mat.* 398, 132419. doi:10.1016/j.conbuildmat.2023.132419

Li, X. G., Wang, P. Q., Qin, J. Y., Liu, Y. X., Qu, Y., Liu, J. J., et al. (2020). Mechanical properties of sintered ceramsite from iron ore tailings affected by two-region structure. *Constr. Build. Mat.* 240, 117919. doi:10.1016/j.conbuildmat.2019.117919

Li, Y. T., Zheng, B. P., Yang, Y. H., Chen, K. J., Chen, X. L., Huang, X., et al. (2022). Soil microbial ecological effect of shale gas oil-based drilling cuttings pyrolysis residue used as soil covering material. *J. Hazard. Mat.* 436, 129231. doi:10.1016/j.jhazmat.2022.129231

Li, Y., Wu, D., Zhang, J., Chang, L., Wu, D., Fang, Z., et al. (2000). Measurement and statistics of single pellet mechanical strength of differently shaped catalysts. *Powder. Technol.* 113, 176–184. doi:10.1016/S0032-5910(00)00231-X

Liang, B., Zhang, M. X., Li, H., Zhao, M., Xu, P. F., and Deng, L. B. (2021). Preparation of ceramic foams from ceramic tile polishing waste and fly ash without added foaming agent. *Ceram. Int.* 47, 23338–23349. doi:10.1016/j.ceramint.2021.05.047

Liu, D. S., Wang, C. Q., Mei, X. D., and Zhang, C. (2018). Environmental performance, mechanical and microstructure analysis of non-fired bricks containing water-based drilling cuttings of shale gas. *Constr. Build. Mat.* 183, 215–225. doi:10.1016/j.conbuildmat.2018.06.107

Liu, W. S., Xiong, X. Y., Zhao, Y. L., Liu, C. Y., Hou, Y. B., and Pu, X. C. (2023). Preparing high-strength and low-density proppants with oil-based drilling cuttings

pyrolysis residues and red mud: process optimization and sintering mechanism. *Fuel* 331, 125777. doi:10.1016/j.fuel.2022.125777

Long-González, D., López-Cuevas, J., Gutiérrez-Chavarría, C. A., Pena, P., Baudin, C., and Turrillas, X. (2009). Synthesis of monoclinic celsian from coal fly ash by using a one-step solid-state reaction process. *Ceram. Int.* 36, 661–672. doi:10.1016/j.ceramint.2009.10.008

Maitra, S., Choudhury, A., Das, H. S., and Pramanik, M. J. (2005). Effect of compaction on the kinetics of thermal decomposition of dolomite under non-isothermal condition. *J. Mat. Sci.* 40, 4749–4751. doi:10.1007/s10853-005-0843-0

Mi, H. C., Yi, L. S., Wu, Q., Xia, J., and Zhang, B. H. (2021). Preparation of high-strength ceramsite from red mud, fly ash, and bentonite. *Ceram. Int.* 47, 18218–18229. doi:10.1016/j.ceramint.2021.03.141

Mi, H. C., Yi, L. S., Wu, Q., Xia, J., and Zhang, H. (2022). A review of comprehensive utilization of red mud. *Waste. Manage.* 40, 1594–1607. doi:10.1177/0734242X221107987

Mishra, A., Siddiqi, H., Kumari, U., Behera, I. D., Mukherjee, S., and Meikap, B. C. (2021). Pyrolysis of waste lubricating oil/waste motor oil to generate high-grade fuel oil: a comprehensive review. *Renew. Sust. Energy Rev.* 150, 111446. doi:10.1016/j.rser.2021.111446

Omar Ahmed, T., and Hassan Assem, A. A. (2021). Behaviour of expanded slate semi-lightweight SCC beams with improved cracking performance and shear capacity. *Structures* 32, 1577–1588. doi:10.1016/j.istruc.2021.03.108

Owens, E., and Santner, R. (2021). Integration of a shoreline response program (SRP) and shoreline assessment surveys into an incident management system for oil spill response. *J. Environ. Manage.* 279, 111637. doi:10.1016/j.jenvman.2020.111637

Pei, J. N., Pan, X. L., Qi, Y. F., Yu, H. Y., and Tu, G. F. (2022). Preparation of ultra-lightweight ceramsite from red mud and immobilization of hazardous elements. *J. Environ. Chem. Eng.* 10, 108157. doi:10.1016/j.jece.2022.108157

Qi, Y. F., Yue, Q. Y., Han, S. X., Yue, M., Gao, B. Y., Yu, H., et al. (2009). Preparation and mechanism of ultra-lightweight ceramics produced from sewage sludge. *J. Hazar. Mat.* 176, 76–84. doi:10.1016/j.jhazmat.2009.11.001

Qin, J., Cui, C., Cui, X. Y., Hussain, A., and Yang, C. M. (2015). Preparation and characterization of ceramsite from lime mud and coal fly ash. *Constr. Build. Mat.* 95, 10–17. doi:10.1016/j.conbuildmat.2015.07.106

Ren, Q., Ren, Y. H., Li, H. H., Wu, X. L., Bai, W., Zheng, J., et al. (2019). Preparation and characterization of high silicon ceramic proppants using low grade bauxite and fly ash. *Mat. Chem. Phys.* 230, 355–361. doi:10.1016/j.matchemphys.2019.04.009

Riley, C. M. (1951). Relation of chemical properties to the bloating of clays. *J. Am. Ceram. Soc.* 34, 121–128. doi:10.1111/j.1151-2916.1951.tb11619.x

Shang, S., Fan, H. H., Li, Y. X., Li, L., and Li, Z. (2022). Preparation of lightweight ceramsite from solid waste using SiC as a foaming agent. *Materials* 15, 325. doi:10.3390/ma15010325

Shih, Y. T., and Jean, J. H. (2017). Low-fire processing of microwave $(Ca_{1-x}Sr_x)(Zr_{1-y}Mn_y)O_3$ dielectric with Li_2O-B_2O_3-SiO_2 glass in H_2/N_2. *Ceram. Int.* 43, S306–S311. doi:10.1016/j.ceramint.2017.05.215

Sun, Y. H., Li, J. S., Chen, Z., Xue, Q., Sun, Q., Zhou, Y. F., et al. (2021). Production of lightweight aggregate ceramsite from red mud and municipal solid waste incineration bottom ash: mechanism and optimization. *Constr. Build. Mat.* 287, 122993. doi:10.1016/j.conbuildmat.2021.122993

Tsai, C. C., Wang, K. S., and Chiou, I. J. (2006). Effect of SiO_2-Al_2O_3-flux ratio change on the bloating characteristics of lightweight aggregate material produced from recycled sewage sludge. *J. Hazard Mat.* 134, 87–93. doi:10.1016/j.jhazmat.2005.10.035

Wang, C. Q., Jin, J. Z., Lin, X. Y., Xiong, D. M., and Mei, X. D. (2017). A study on the oil-based drilling cutting pyrolysis residue resource utilization by the exploration and development of shale gas. *Environ. Sci. Pollut. R.* 24, 17816–17828. doi:10.1007/s11356-017-9199-7

Wang, C. Q., Lin, X. Y., Mei, X. D., and Luo, X. G. (2019). Performance of non-fired bricks containing oil-based drilling cuttings pyrolysis residues of shale gas. *J. Clean. Prod.* 206, 282–296. doi:10.1016/j.jclepro.2018.09.128

Wang, D., Huang, J. L., Peng, H. T., and Huang, J. L. (2014). Sinterability and expansion property of ceramsite made with lead-zinc mine tailings. *Des. Manuf. Mechatron.* 551, 23–27. doi:10.4028/www.scientific.net/AMM.551.23

Wang, L. K., Shao, Y. L., Zhao, Z. L., Chen, S., and Shao, X. H. (2020). Optimized utilization studies of dredging sediment for making water treatment ceramsite based on an extreme vertex design. *J. Water. Process. Eng.* 38, 101603. doi:10.1016/j.jwpe.2020.101603

Xie, X., Wang, D., Liu, D., Zhang, X., and Oeser, M. (2016). Investigation of synthetic, self-sharpening aggregates to develop skid-resistant asphalt road surfaces. *Wear* 348-349, 52–60. doi:10.1016/j.wear.2015.11.022

Xiong, D. M., and Wang, C. Q. (2021). Physical characteristics and environmental risks assessment of oil-based drilling cuttings residues used for subgrade materials. *J. Clean. Prod.* 323, 129152. doi:10.1016/j.jclepro.2021.129152

Yang, H., Liu, Y. L., Bai, G. L., Feng, Z., Zhang, Y., and Xia, S. B. (2022). Solidification and utilization of water-based drill cuttings to prepare ceramsite proppant with low-density and high performance. *Pet. Sci.* 19, 2314–2325. doi:10.1016/j.petsci.2022.06.006

Yang, H. Y., Li, E. Z., Yang, H. C., He, H. C., and Zhang, R. S. (2018). Synthesis of $Zn_{0.5}Ti_{0.5}NbO_4$ microwave dielectric ceramics with Li_2O-B_2O_3-SiO_2 glass for LTCC application. *Int. J. Appl. Glas. Sci.* 9, 392–402. doi:10.1111/ijag.12334

Yang, Y. F., Inamori, Y. H., Ojima, H., Machii, H., and Shimizu, Y. (2005). Development of an advanced biological treatment system applied to the removal of nitrogen and phosphorus using the sludge ceramics. *Water. Res.* 39, 4859–4868. doi:10.1016/j.watres.2004.10.019

Yashima, S., Kanda, Y., and Sano, S. (1987). Relationships between particle size and fracture energy or impact velocity required to fracture as estimated from single particle crushing. *Powder. Technol.* 51, 277–282. doi:10.1016/0032-5910(87)80030-X

Yoon, K. H., Park, M. S., Cho, J. Y., and Kim, E. S. (2003). Effect of B_2O_3-Li_2O on microwave dielectric properties of $(Ca_{0.275}Sm_{0.4}Li_{0.25})TiO_3$ ceramics. *J. Eur. Ceram. Soc.* 23, 2423–2427. doi:10.1016/s0955-2219(03)00164-x

Zhao, D., Gao, Y. N., Nie, S., Liu, Z. C., Wang, F. Z., Liu, P., et al. (2018). Self-assembly of honeycomb-like calcium-aluminum-silicate-hydrate (C-A-S-H) on ceramsite sand and its application in photocatalysis. *Chem. Eng. J.* 344, 583–593. doi:10.1016/j.cej.2018.03.074

Zhuo, L., Xxin, G. R., Yong, W. X., Sshu, F. C., and sheng, L. R. (2023). Construction ceramsite from low-silicon red mud: design, preparation, and sintering mechanism analysis. *Process. Saf. Environ.* 176, 166–179. doi:10.1016/j.psep.2023.06.017